Supplementary Material: Bend-Induced Twist Waves and the Structure of Nucleosomal DNA

Enrico Skoruppa,[1] Stefanos K. Nomidis,[1,2] John F. Marko,[3] and Enrico Carlon[1]

[1] *KU Leuven, Institute for Theoretical Physics, Celestijnenlaan 200D, 3001 Leuven, Belgium*
[2] *Flemish Institute for Technological Research (VITO), Boeretang 200, B-2400 Mol, Belgium*
[3] *Department of Physics and Astronomy, and Department of Molecular Biosciences, Northwestern University, Evanston, Illinois 60208, USA*

(Dated: July 30, 2018)

CONTENTS

I. DETAILS OF THE ANALYTICAL SOLUTION

In the main text we presented an energy-minimization calculation for bent DNA, leading to [Eqs. (4) of main text]

$$\Omega_1 = \frac{\mu \sin(\omega_0 s)}{A_1}, \quad \Omega_2 = \frac{\mu \cos(\omega_0 s)}{A_2 - G^2/C}, \quad \Omega_3 = -\frac{G}{C}\,\Omega_2. \tag{S1}$$

These were obtained by introducing the constraint $-\mu \int \boldsymbol{\Omega}_b \cdot \widehat{\mathbf{x}}\, \mathrm{d}s$, which favors the alignment of the bending vector $\boldsymbol{\Omega}_b = \Omega_1 \widehat{\mathbf{e}}_1 + \Omega_2 \widehat{\mathbf{e}}_2$ along a fixed unit vector $\widehat{\mathbf{x}}$. Figure S1 shows the 3d shape obtained from the analytical solution (S1).

The constraint, however, does not force the elastic rod to completely lie on the plane orthogonal to $\widehat{\mathbf{x}}$, but it is sufficiently flexible to allow for off-planar conformations. This can be shown by decomposing the bending vector $\boldsymbol{\Omega}_b$ as follows

$$\begin{aligned} \boldsymbol{\Omega}_b &= [\widehat{\mathbf{x}}\,(\boldsymbol{\Omega}_b \cdot \widehat{\mathbf{x}})] + [\boldsymbol{\Omega}_b - \widehat{\mathbf{x}}\,(\boldsymbol{\Omega}_b \cdot \widehat{\mathbf{x}})] \\ &= [\widehat{\mathbf{x}}\,(\boldsymbol{\Omega}_b \cdot \widehat{\mathbf{x}})] + [\boldsymbol{\Omega}_b\,(\widehat{\mathbf{x}} \cdot \widehat{\mathbf{x}}) - \widehat{\mathbf{x}}\,(\boldsymbol{\Omega}_b \cdot \widehat{\mathbf{x}})] \\ &= (\widehat{\mathbf{x}} \cdot \boldsymbol{\Omega}_b)\,\widehat{\mathbf{x}} \;\; + (\widehat{\mathbf{x}} \times \boldsymbol{\Omega}_b) \times \widehat{\mathbf{x}} \end{aligned} \tag{S2}$$

ÏĹ i.e. into a parallel and perpendicular component to $\widehat{\mathbf{x}}$. The corresponding lengths of the two components are

$$\kappa_{\parallel} = |\boldsymbol{\Omega}_b \cdot \widehat{\mathbf{x}}| = \mu \left[\frac{1}{l_b} + \frac{\cos(2\omega_0 s)}{l_d} \right] \tag{S3}$$

and

$$\kappa_{\perp} = \|(\widehat{\mathbf{x}} \times \boldsymbol{\Omega}_b) \times \widehat{\mathbf{x}}\| = \|\boldsymbol{\Omega}_b \times \widehat{\mathbf{x}}\| = \frac{\mu}{l_d} \left|\sin(2\omega_0 s)\right|, \tag{S4}$$

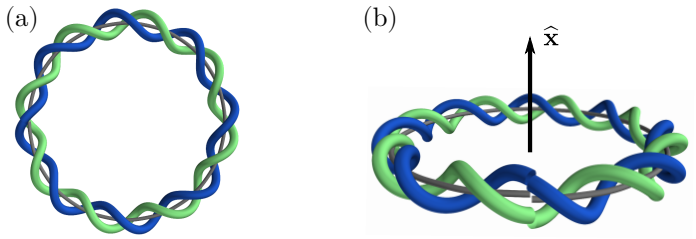

FIG. S1. (a) Top view: Spatial configuration of the analytical ground-state solution for a DNA minicircle [Eqs. (S1)], obtained by numerically solving Eq. (S11). (b) Side view: In general Eqs. (S1) do not describe a closed circular shape, however, by properly choosing the total length and μ, one can minimize the mismatch at the boundary. The gray line represents the molecular axis, extracted from the tangent vector $\widehat{\mathbf{e}}_3$, whereas the double helix (green and blue lines) was generated from the triad vector $\widehat{\mathbf{e}}_1$. The length of the minicircle was 29 nm, corresponding to 85 base pairs, and the remaining parameters were chosen as $A_1 = 80$ nm, $A_2 = 50$ nm, $C = 110$ nm, $G = 40$ nm and $\omega_0 = 1.75$ nm^{-1}.

where we have used the relations $\widehat{\mathbf{e}}_1 \cdot \widehat{\mathbf{x}} = \sin(\omega_0 s)$, $\widehat{\mathbf{e}}_2 \cdot \widehat{\mathbf{x}} = \cos(\omega_0 s)$, $\widehat{\mathbf{e}}_1 \times \widehat{\mathbf{x}} = \cos(\omega_0 s)\widehat{\mathbf{z}}$, $\widehat{\mathbf{e}}_2 \times \widehat{\mathbf{x}} = -\sin(\omega_0 s)\widehat{\mathbf{z}}$, with $\widehat{\mathbf{z}}$ a unit vector orthogonal to the plane on which $\widehat{\mathbf{e}}_1$, $\widehat{\mathbf{e}}_2$ and $\widehat{\mathbf{x}}$ lie (see Fig. 1 of the main text). The two lengths l_d and l_b are defined from the relations

$$\frac{1}{l_d} \equiv \frac{1}{2}\left(\frac{1}{A_2 - G^2/C} - \frac{1}{A_1}\right), \tag{S5}$$

$$\frac{1}{l_b} \equiv \frac{1}{2}\left(\frac{1}{A_2 - G^2/C} + \frac{1}{A_1}\right), \tag{S6}$$

(recall that the elastic constants as defined in Eq. 2 of the main text have the dimension of lengths). It is interesting to notice that l_b, as defined in Eq. (S6), is also the persistence length of the model, i.e. the characteristic length obtained from the decay of the tangent-tangent correlation function in a fluctuating open fragment [1]. Note, finally, that Eq. (S3) allows to fix the value of the Lagrange multiplier μ. Consider a bent (quasi-)planar rod with radius of curvature R. One has

$$\frac{1}{R} = \langle \kappa_\parallel \rangle = \frac{\mu}{l_b}, \tag{S7}$$

from which we get $\mu = l_b/R$. Moreover, that the sum of the amplitudes of the bending waves is equal to the simple expression

$$\max\{\Omega_1\} + \max\{\Omega_2\} = \frac{2\mu}{l_b} = \frac{2}{R}, \tag{S8}$$

as can be seen by combining Eqs. (S1), (S6) and (S7).

II. ALTERNATIVE CONSTRAINT

In the main text we introduced a Lagrange multiplier to induce bending, while forcing the rod to lie on average on a plane. Here we discuss an alternative constraint, which turns out to be less adequate for our problem. Nonetheless it is useful to illustrate some issues arising when a generic bending is enforced. Consider the following energy

$$\beta\widehat{E} = \frac{1}{2}\int_0^L \left[A_1\Omega_1^2 + A_2\Omega_2^2 + C\Omega_3^2 + 2G\Omega_2\Omega_3 - 2\mu\kappa\right] \mathrm{d}s, \tag{S9}$$

where $\kappa \equiv (\Omega_1^2 + \Omega_2^2)^{1/2}$ is the curvature, and $\mu > 0$ a Lagrange multiplier. Minimization of Eq. (S9) leads to the following s-independent values

$$\Omega_1 = 0, \qquad \Omega_2 = \frac{\mu}{A_2 - G^2/C}, \qquad \Omega_3 = -\frac{G}{C}\Omega_2 = -\frac{\mu G}{A_2 C - G^2}. \tag{S10}$$

Notice that $\Omega_1 = 0$, i.e. there is no bending along the hard axis (recall that $A_1 > A_2$) is zero everywhere, since the direction of bending is unconstrained. In order to determine the shape of the rod corresponding to the above solution,

we plug Eqs. (S10) into the differential

$$\frac{\mathrm{d}\widehat{\mathbf{e}}_i}{\mathrm{d}s} = (\boldsymbol{\Omega} + \omega_0 \widehat{\mathbf{e}}_3) \times \widehat{\mathbf{e}}_i, \tag{S11}$$

and solving for $\widehat{\mathbf{e}}_i$ we obtain:

$$\widehat{\mathbf{e}}_1(s) = \cos(\Lambda s)\,\widehat{\mathbf{y}} + \sin(\Lambda s)\,\widehat{\mathbf{z}}, \tag{S12}$$
$$\widehat{\mathbf{e}}_2(s) = R\Lambda\,\widehat{\mathbf{x}} - \Gamma \sin(\Lambda s)\,\widehat{\mathbf{y}} + \Gamma \cos(\Lambda s)\,\widehat{\mathbf{z}}, \tag{S13}$$
$$\widehat{\mathbf{e}}_3(s) = \Gamma\,\widehat{\mathbf{x}} + R\Lambda \sin(\Lambda s)\,\widehat{\mathbf{y}} - R\Lambda \cos(\Lambda s)\,\widehat{\mathbf{z}}, \tag{S14}$$

where we have defined

$$\Lambda \equiv \sqrt{\Omega_2^2 + (\Omega_3 + \omega_0)^2}, \qquad R \equiv \frac{\Omega_2}{\Lambda^2}, \qquad \Gamma \equiv \frac{\Omega_3 + \omega_0}{\Lambda}. \tag{S15}$$

Finally, integrating the tangent vector $\widehat{\mathbf{e}}_3$ yields the position vector

$$\mathbf{r}(s) = \int_0^s \mathrm{d}s'\,\widehat{\mathbf{e}}_3(s') = \Gamma s\,\widehat{\mathbf{x}} + R\left[1 - \cos(\Lambda s)\right]\,\widehat{\mathbf{y}} - R\sin(\Lambda s)\,\widehat{\mathbf{z}}, \tag{S16}$$

which describes a superhelix of radius R and pitch $2\pi\Gamma/\Lambda$. The problem with this procedure is that it imposes a bending without specifying a particular direction. To avoid bending along the stiff direction the rod forms a superhelical conformation. As we wish to generate a mainly planar bent conformation, the constraint introduced in (S9) is not adequate for our problem.

III. FIXED CURVATURE AND TORSION

We can also obtain twist waves following the approach described in Ref. [2], which uses the Frenet-Serret variables. $\{\widehat{\mathbf{e}}_1, \widehat{\mathbf{e}}_2, \widehat{\mathbf{e}}_3\}$ is the material frame (also known as Darboux frame) of the elastic rod. An alternative description is obtained by the Frenet-Serret frame $\{\widehat{\mathbf{t}}, \widehat{\mathbf{n}}, \widehat{\mathbf{b}}\}$ formed by the tangent $\widehat{\mathbf{t}}(= \widehat{\mathbf{e}}_3)$, the normal $\widehat{\mathbf{n}}$ and the binormal $\widehat{\mathbf{b}}$. This frame is constructed from derivatives of the unit tangent vector as follows:

$$\frac{\mathrm{d}\widehat{\mathbf{t}}}{\mathrm{d}s} = \kappa\widehat{\mathbf{n}}, \qquad \frac{\mathrm{d}\widehat{\mathbf{n}}}{\mathrm{d}s} = -\kappa\widehat{\mathbf{t}} + \tau\widehat{\mathbf{b}}, \qquad \frac{\mathrm{d}\widehat{\mathbf{b}}}{\mathrm{d}s} = -\tau\widehat{\mathbf{n}}, \tag{S17}$$

where κ is the curvature, defined below Eq. (S9), and τ the torsion. The two frames are connected to each other by a rotation by an angle ϕ around the common tangent vector. The relation between Darboux variables Ω_i and Frenet-Serret vatriables κ, τ and ϕ is

$$\Omega_1 = \kappa \sin\phi, \qquad \Omega_2 = \kappa\cos\phi, \qquad \Omega_3 = \phi_s - \omega_0 + \tau, \tag{S18}$$

where $\phi_s \equiv \mathrm{d}\phi/\mathrm{d}s$. In terms of Frenet-Serret variables the energy functional hence becomes

$$\beta E = \frac{1}{2}\int_0^L \mathrm{d}s\left[A\kappa^2 - \varepsilon\kappa^2\cos 2\phi + C(\phi_s - \bar{\omega})^2 + 2G\kappa\,(\phi_s - \bar{\omega})\cos\phi\right], \tag{S19}$$

where we have introduced $A \equiv (A_1 + A_2)/2$, $\varepsilon \equiv (A_1 - A_2)/2$ and $\bar{\omega} = \omega_0 - \tau$. Similarly to Ref. [2], we minimize the energy of the rod for fixed κ and τ. The associated Euler-Lagrange equation for ϕ is [2]

$$\phi_{ss} = \frac{\varepsilon\kappa^2}{C}\sin 2\phi + \frac{G\kappa\bar{\omega}}{C}\sin\phi. \tag{S20}$$

Note that $\phi_s\cos\phi$ in Eq. (S19) does not contribute to the Euler-Lagrange equation, as it can be integrated out yielding a boundary term. Interpreting the coordinate s as time, the previous equation can be viewed as Newton's equation of motion of a particle moving in a periodic potential. Integrating once the previous equation one gets [2]

$$\phi_s^2 = \omega^2 - \frac{\varepsilon\kappa^2}{C}\cos 2\phi - \frac{2G\kappa\bar{\omega}}{C}\cos\phi, \tag{S21}$$

with ω an integration constant (in the mechanical analogy this relation expresses the conservation of energy).

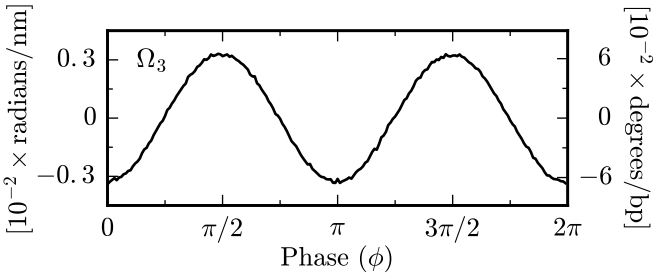

FIG. S2. Plot of Ω_3 from simulations of oxDNA1. This model has symmetric grooves, hence one expects $G = 0$. In this case Eq. (S24) predicts weaker twist waves with frequency $2\omega_0$. The data shown in the plot support this conclusion.

Let us first consider the case of vanishing torsion $\tau = 0$, which corresponds to a planar curve. In this case $\bar{\omega} = \omega_0$. As assumed in the main text, for a weakly bent rod we expect that $\phi \approx \omega_0 s$, with a weak modulation due to the periodic potential. Replacing $\omega = \omega_0$ in Eq. (S21) we get for the excess twist density

$$\Omega_3 = \phi_s - \omega_0 = \omega_0 \sqrt{1 - \frac{\varepsilon\kappa^2}{C\omega_0^2}\cos 2\phi - \frac{2G\kappa}{C\omega_0}\cos\phi} - \omega_0 \approx -\frac{G\kappa}{C}\cos(\omega_0 s), \tag{S22}$$

where we have expanded to lowest order in κ/ω_0 and used the lowest-order value $\phi = \omega_0 s + \mathcal{O}(\kappa/\omega_0)$. Note that this solution is identical to Eq. (4) of the main text. There is however, a crucial difference in the bending amplitudes. In particular, the bending components are found to be

$$\Omega_1 \approx \kappa \sin(\omega_0 s), \qquad \Omega_2 \approx \kappa \cos(\omega_0 s). \tag{S23}$$

i.e. the two waves have equal amplitudes, which naturally follows from the constraint of imposing a constant κ. As shown in the comparison with simulations, the DNA attains lower energy by having higher bending amplitudes along the easy bending direction. There is an interesting prediction one can obtain from Eq. (S22). By setting $G = 0$ in Eq. (S22) and performing again a κ/ω_0 expansion we obtain

$$\Omega_3 \approx -\frac{\varepsilon\kappa^2}{2C\omega_0}\cos(2\omega_0 s), \tag{S24}$$

which is again a twist wave, albeit with much lower amplitude (being higher order in κ/ω_0). The wave is predicted to have double the frequency of that induced by twist-bend coupling. Figure S2 shows a zoom-in of the Ω_3 data for an oxDNA1 minicircle (same data as the lowest panel of Fig. 2 in the main paper), corresponding to the case $G \approx 0$ and $\varepsilon \neq 0$, which indeed show a frequency doubling of the twist waves.

Note that we can extend the solution to a fixed non-vanishing torsion $\tau \neq 0$. In this case one needs to replace ω_0 with $\omega_0 - \tau$ in Eqs. (S22)-(S23). For nucleosomal DNA the ratio between the average torsion and intrinsic twist density has been estimated to be $\langle\tau\rangle/\omega_0 \approx 0.01$ [3], hence the torsion can be safely set to zero.

IV. OXDNA

Details of Simulations – oxDNA is a coarse-grained model of DNA, consisting of a series of rigid nucleotides. Excluded-volume effects, backbone bonds, hydrogen interactions, stacking and cross-stacking are modelled by means of pairwise interactions. In the original version (oxDNA1) the double helix was perfectly symmetric [4], with groove asymmetry being introduced in a subsequent version (oxDNA2) [5]. This is also illustrated at the top of Fig. S3.

The sampling was performed using NVE molecular dynamics simulations, together with an Andersen-like thermostat. In brief this approach consists of a series of repeated cycles: First Newton's equations of motion are integrated several steps, and then the momenta of some particles (chosen at random) are reset from a Maxwell distribution. This process is repeated many times, and eventually leads to equilibration of the system. As we are interested in the ground-state configuration, the simulations were performed at a low temperature (10 K). At this temperature one generates configurations close to the ground state, but with enough thermal fluctuation to allow generation of new configurations (in total 3×10^5 independent conformations were generated).

Comparison with theory – Figure S3 shows a comparison between low-temperature simulations of oxDNA minicircles (solid lines) and our analytical result [Eqs. (4) of main text, shown with dashed lines]. It should be stressed that

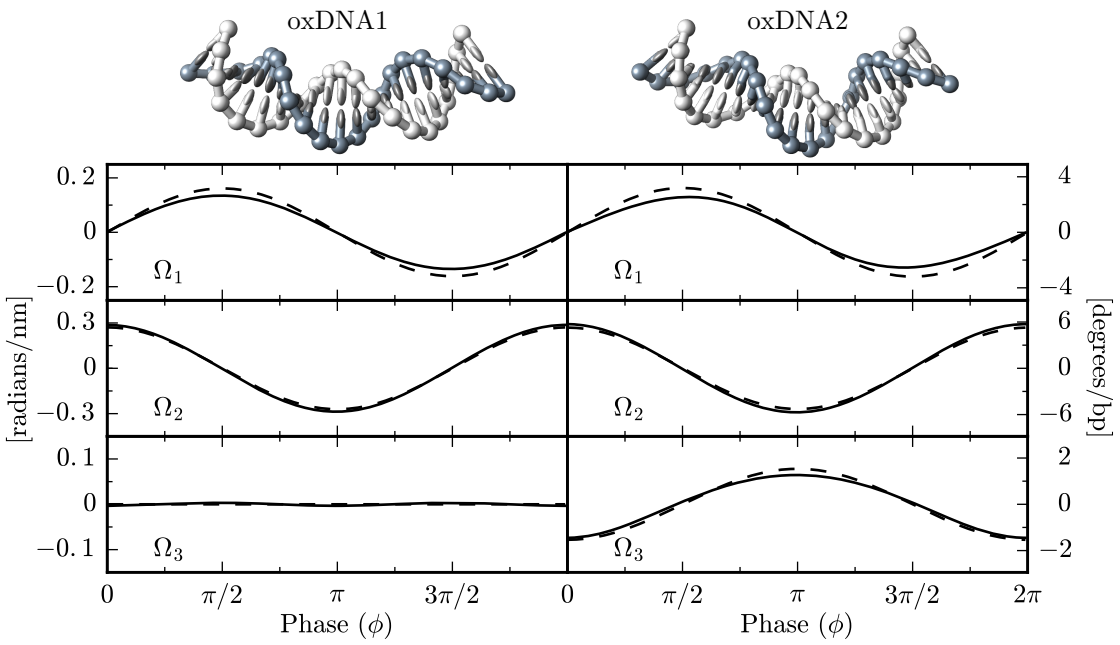

FIG. S3. Comparison between the analytical result of the main text [Eqs. (4), plotted with dashed lines] and oxDNA simulations (solid lines). In both oxDNA1 (left) and oxDNA2 (right) the agreement with the theory is good. The two vertical axes show the angle density in different units, while the horizontal axis corresponds to the local phase ϕ of each point. Top: Visual representation of the two oxDNA models, with their respective cross-sectional views.

this comparison contains no free parameters, as the radius, which determines μ, and the elastic parameters, which set the amplitudes, are fixed. In particular, we used $R_{\text{mean}} \approx 4.6$ nm for the radius, corresponding to that of a perfect minicircle of length 85 bp $\approx$ 29 nm. The stiffness parameters were taken from the analysis of oxDNA elasticity of Ref. [6]: $A_1 = 51$ nm, $A_2 = 30$ nm, $C = 77$ nm and $G = 0$ for oxDNA1, and $A_1 = 51$ nm, $A_2 = 37$ nm, $C = 74$ nm and $G = 22$ nm for oxDNA2. These are the local stiffness parameters associated to the deformation at the single base pair level ($m = 1$ data in supplementary Fig. S3 of Ref. [6]). Simulations have shown that stiffness parameters at a distance of a single base pair differ from the asymptotic continuum limit value [6]. Figure S3 reveals an overall good agreement between oxDNA simulations and theory. The small deviations probably arise from some additional interactions (e.g. stretching and higher-order terms) than those considered in the energy functional [Eq. (2) of main text]. As already remarked in Fig. 2 of the main text, one notices the absence of twist waves in oxDNA1 (left) and their presence in oxDNA2 (right). This is a consequence of twist-bend coupling, which has been shown to arise from the groove asymmetry of the DNA double helix [2]. In fact, it was recently found that the magnitude of twist-bend coupling is negligible in oxDNA1 and considerable in oxDNA2 [6].

V. MONTE CARLO SIMULATIONS

In order to independently test our analytical results [Eqs. (4) of main text], we additionally performed low-temperature (10 K) Monte Carlo simulations of a simple, circular-DNA model. The model consists of 84 beads representing each base pair, and each carrying a frame of three orthogonal unit vectors $\{\widehat{\mathbf{e}}_1, \widehat{\mathbf{e}}_2, \widehat{\mathbf{e}}_3\}$. The ground state for such an open chain is a straight configuration (i.e. all $\widehat{\mathbf{e}}_3$ vectors are parallel), with a 34-degree rotation between neighboring sets of vectors $\{\widehat{\mathbf{e}}_1, \widehat{\mathbf{e}}_2\}$, corresponding to the intrinsic twist density of the double helix. The energy of a conformation is obtained by discretizing the continuum energy model

$$\beta E = \frac{1}{2} \int_0^L \left(A_1 \Omega_1^2 + A_2 \Omega_2^2 + C \Omega_3^2 + 2G \Omega_2 \Omega_3 \right) \mathrm{d}s. \tag{S25}$$

For the generation of new configurations we selected a bead at random and updated its position and triad vector orientation, while keeping the other beads fixed. The acceptance probability was calculated with the Metropolis-Hastings algorithm. The advantage of this model over oxDNA is that the stiffness constants A_1, A_2, C and G are input parameters, allowing us to directly compare with the analytical results of the main text. For our purposes we

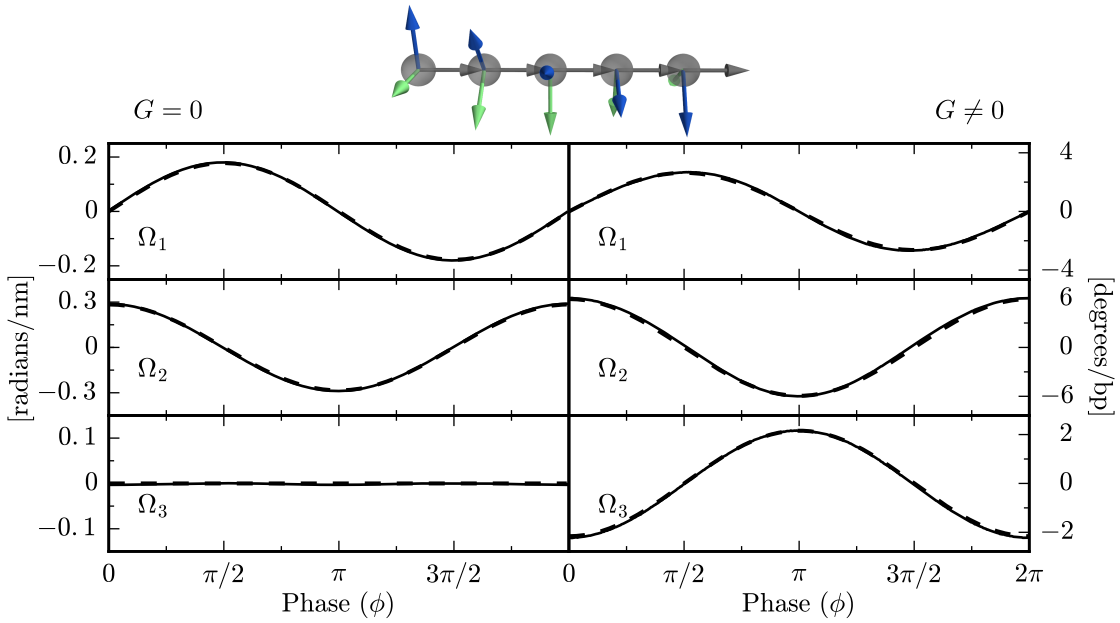

FIG. S4. Comparison between the analytical result of the main text [Eqs. (4), plotted with dashed lines] and Monte Carlo simulations (solid lines), with zero (left) and nonzero (right) twist-bend coupling. Observable twist waves only appear in the latter case, in quantitative agreement with the theoretical predictions. The two vertical axes show the angle density in different units, while the horizontal axis corresponds to the local phase ϕ of each point. Top: Schematic representation of the computer model, consisting by a series of triads.

used: $A_1 = 80$ nm, $A_2 = 50$ nm, $C = 110$ nm, and G either 0 or 40 nm, so as to isolate the effect of twist-bend coupling. Using Monte Carlo simulations of this model, one can directly put the analytical results [Eqs. (4) of main text and Eqs. (S1)] to the test. Figure S4 shows a comparison between the obtained values of Ω_i (solid lines) and the analytical results (dashed lines). For the latter, μ was estimated using the input stiffness parameters of the model, and the expected radius $R \approx 4.3$ nm for a perfect circular configuration, in Eqs. (S6) and (S7). Both in presence and absence of twist-bend coupling (left and right plots, respectively) our analysis reveals an excellent agreement with the theory.

VI. NUCLEOSOMAL DNA DATA

Figure 3 of the main text shows the bending and twist waves, obtained by averaging over 145 available nucleosomal structures from X-ray crystallographic data. Here we explain the averaging procedure in more detail, and show some individual data from selected files. Finally, in Table SI we present a full list of the freely-available PDB [7] files included in our analysis.

For the extraction of the deformation parameters Ω_1, Ω_2 and Ω_3 at each site, we used the Curves+ freely-distributed nucleic-acid software [8], and we subsequently computed the discrete Fourier spectrum of the resulting values (as shown in Fig. S5). Since the spectrum Ω_2 was the only one that consistently yielded a clear, dominant peak at the same frequency, the computation of each phase was based on it. As also mentioned in the main text, we estimated the frequency ω_0 of each wave from the dominant peak, and the *global* phase ψ from the ratio between the real and imaginary parts of the Fourier component corresponding to that frequency. This way, the *local* phase ϕ_n associated with each site n was computed as $\phi_n =$ mod $(\psi + na\omega_0, 2\pi)$, where $a = 0.34$ nm is the base pair separation. Finally, in order to acquire sufficient statistics, the resulting Ω vs. ϕ data were binned and averaged.

The aforementioned features of nucleosomal DNA, namely the emergence of bending-induced twist waves, are even visible in most individual nucleosomal data. Figure S5 shows such an example, with a clear, dominant frequency in the Fourier spectrum of Ω_3 at ω_0, and a phase difference of π with respect to the Ω_2 wave, again in agreement with our analytical results.

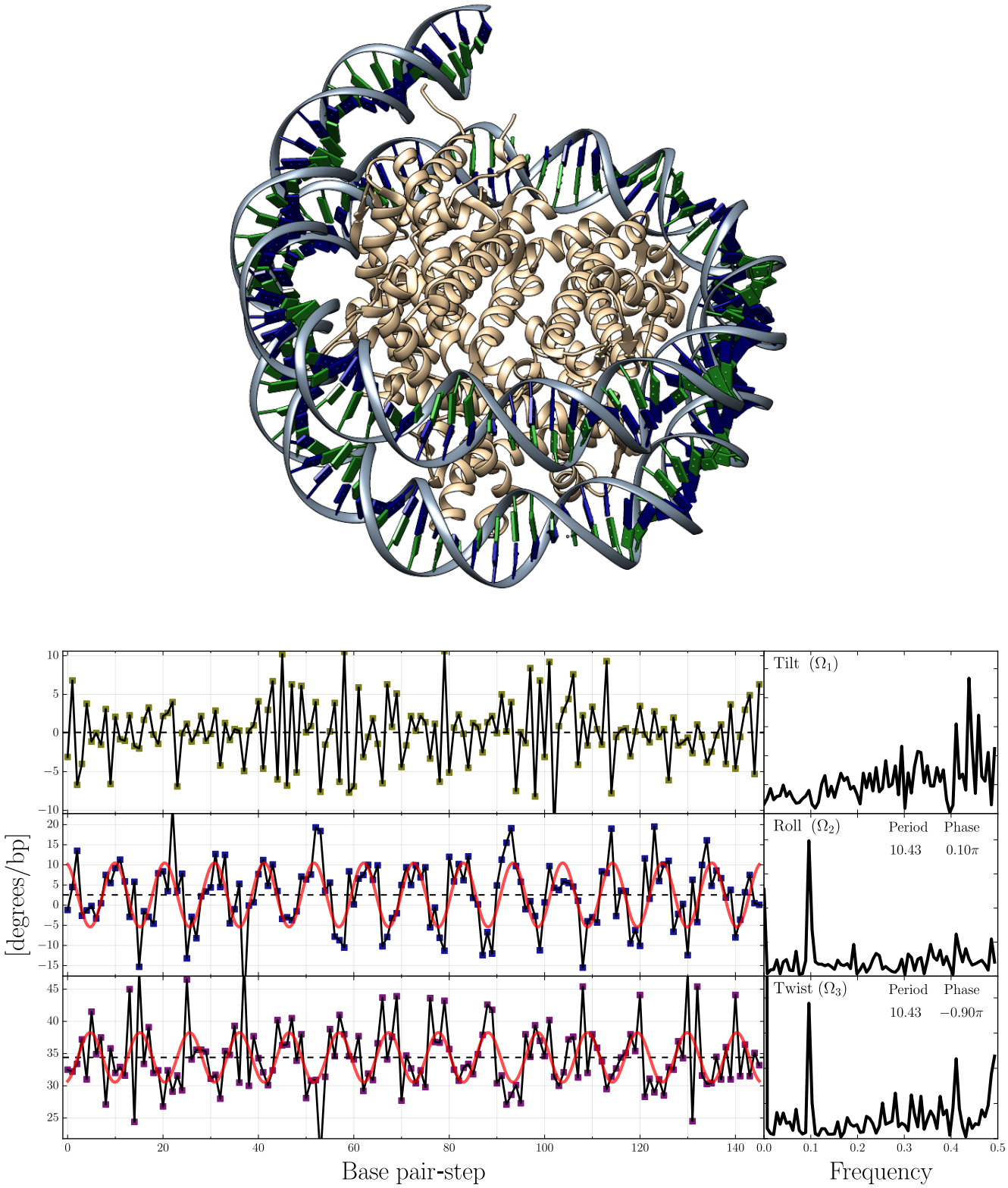

FIG. S5. Individual example of the analysis performed on 145 nucleosomal data. Top: Graphical representation of the nucleosome configuration. Bottom: Plot of the rotational degrees of freedom (tilt, roll and twist from top to bottom) extracted with Curves+, as a function of the base-pair step. The dashed lines indicate the mean values, whereas the red lines show a harmonic fit to the data. The plots on the right are the corresponding Fourier spectra. These plots were obtained from the 5OMX [9] nucleosomal PDB file.

TABLE SI. List of PDB files used in our analysis, taken from the Protein Data Bank (PDB). All structures show a strong peak at ω_0 in the Fourier spectrum of Ω_2 and Ω_3. Only a small fraction (indicated by an asterisk (*)) exhibit a clear peak at ω_0 in Ω_1 and were included in the computation of the thin line of Fig. 3 (main text).

1AOI	1P3I	3A6N	3AZN	3MGS*	3W98	4R8P	5AY8	5F99	5XF3
1EQZ	1P3K*	3AFA	3B6F*	3MNN	3W99	4WU8	5B0Y	5GSU	5XF4
1F66	1P3L	3AN2	3B6G*	3MVD	3WA9	4WU9	5B0Z	5GT0	5XF5
1ID3	1P3M	3AV1	3C1B	3O62	3WAA	4X23*	5B1L	5GT3	5XF6
1KX3	1P3O*	3AV2	3C1C	3REH	3WKJ	4XUJ	5B1M	5GTC	6BUZ*
1KX4	1P3P*	3AYW	3KUY	3REI	3WTP	4XZQ	5B2I	5GXQ	6C0W*
1KX5	1S32	3AZE	3KWQ	3REJ	3X1S	4YS3	5B31	5KGF*	6ESF*
1M18	1U35*	3AZF	3KXB	3REK	3X1T	4Z5T	5B32	5MLU*	6ESG*
1M19	1ZLA	3AZG	3LEL	3REL	3X1U	4Z66	5B33	5O9G*	6ESH*
1M1A	2CV5	3AZH	3LJA	3TU4*	3X1V	5AV5	5B40	5OMX	6ESI*
1P34*	2F8N	3AZI	3LZ0	3UT9	4JJN	5AV6	5CP6	5ONG	
1P3A	2FJ7	3AZJ	3LZ1*	3UTA	4KGC	5AV8	5CPI	5ONW*	
1P3B	2NQB	3AZK	3MGP	3UTB	4KUD	5AV9	5DNM	5X0X	
1P3F	2NZD	3AZL	3MGQ	3W96	4LD9*	5AVB	5DNN	5X0Y*	
1P3G	2PY0	3AZM	3MGR*	3W97	4QLC	5AVC	5E5A	5X7X	

VII. COMPARISON WITH OTHER WORK

In a previous work [10] a different type of constraint was used for the minimization of an elastic rod model with anisotropic bending (as $G = 0$ in their model, there are no manifest twist waves). The minimization scheme of Ref. [10] gives

$$\Omega_1 = \frac{\lambda \sin(\omega_0 s)}{A + A' \cos(2\omega_0 s)} \qquad \Omega_2 = \frac{\lambda \cos(\omega_0 s)}{A + A' \cos(2\omega_0 s)}, \tag{S26}$$

where λ is a Lagrange multiplier and $A \equiv (A_1 + A_2)/2$, $A' \equiv (A_1 - A_2)/2$. This solution represents modulated sinusoidal waves which differ from Eqs. (S1). Fig. S6 shows a comparison betweeen the two results. One observes some deviations between the two and as both contain some approximations a priori it is not clear which one is more suitable. The results of the Monte Carlo simulations shown in Fig. S4 however match the solution proposed in this work extremely well.

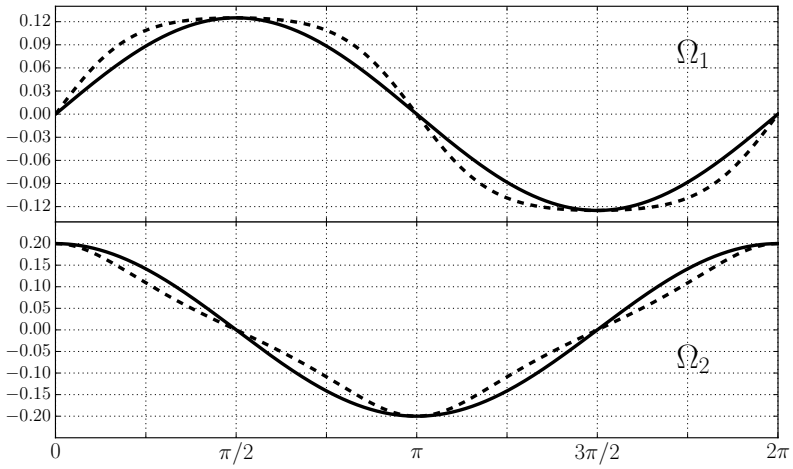

FIG. S6. Comparison between the expression for Ω_1 and Ω_2 found in this work (solid line) and in Ref. [10] (dashed line).

[1] In Ref. [11] it was shown that the bending persistence length is [Eq. (3) of Ref. [11]]

$$l_b = \kappa_b = A\frac{1-\frac{\varepsilon^2}{A^2}-\frac{G^2}{AC}\left(1+\frac{\varepsilon}{A}\right)}{1-\frac{G^2}{2AC}},$$

with $A = (A_1 + A_2)/2$ and $\varepsilon = (A_1 - A_2)/2$. A simple manipulation of the above expression yields Eq. (S6).
[2] J. F. Marko and E. D. Siggia, Macromolecules **27**, 981 (1994).
[3] F. Mohammad-Rafiee and R. Golestanian, Phys. Rev. Lett. **94**, 238102 (2005).
[4] P. Šulc, F. Romano, T. E. Ouldridge, L. Rovigatti, J. P. K. Doye, and A. A. Louis, J. Chem. Phys. **137**, 135101 (2012).
[5] B. E. Snodin, F. Randisi, M. Mosayebi, P. Šulc, J. S. Schreck, F. Romano, T. E. Ouldridge, R. Tsukanov, E. Nir, and A. A. Louis, J. Chem. Phys. **142**, 234901 (2015).
[6] E. Skoruppa, M. Laleman, S. K. Nomidis, and E. Carlon, J. Chem. Phys. **146**, 214902 (2017).
[7] H. M. Berman, J. Westbrook, Z. Feng, G. Gilliland, T. N. Bhat, H. Weissig, I. N. Shindyalov, and P. E. Bourne, Nucl. Acids Res. **28**, 235 (2000).
[8] R. Lavery, M. Moakher, J. H. Maddocks, D. Petkeviciute, and K. Zakrzewska, Nucl. Acids Res. **37**, 5917 (2009).
[9] T. D. Frouws, P. D. Barth, and T. J. Richmond, J. Mol. Biol. **430**, 45 (2018).
[10] F. Mohammad-Rafiee and R. Golestanian, J. Phys.: Cond. Matt. **17**, S1165 (2005).
[11] S. K. Nomidis, F. Kriegel, W. Vanderlinden, J. Lipfert, and E. Carlon, Phys. Rev. Lett. **118**, 217801 (2017).